APL Photonics

RESEARCH ARTICLE | MAY 09 2024

Extended short-wave infrared high-speed all-GeSn PIN photodetectors on silicon

Special Collection: Mid-IR Photonics

M. R. M. Atalla ; C. Lemieux-Leduc ; S. Assali ; S. Koelling ; P. Daoust ; O. Moutanabbir

Check for updates

APL Photonics 9, 056103 (2024)
https://doi.org/10.1063/5.0197018

View Online
Export Citation

26 September 2024 16:56:28

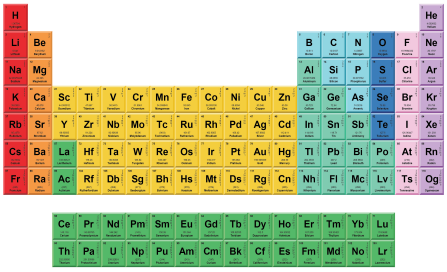

AMERICAN ELEMENTS
THE MATERIALS SCIENCE MANUFACTURER®
Now Invent.™
27th ANNIVERSARY 1997 - 2024
American Elements Opens a World of Possibilities
...Now Invent!
www.americanelements.com
© 2001-2024, American Elements is a U.S. Registered Trademark

AIP Publishing

APL Photonics ARTICLE pubs.aip.org/aip/app

Extended short-wave infrared high-speed all-GeSn PIN photodetectors on silicon

Cite as: APL Photon. 9, 056103 (2024); doi: 10.1063/5.0197018
Submitted: 11 January 2024 • Accepted: 24 April 2024 •
Published Online: 9 May 2024

View Online Export Citation CrossMark

M. R. M. Atalla, C. Lemieux-Leduc, S. Assali, S. Koelling, P. Daoust, and O. Moutanabbir[a)]

AFFILIATIONS

Department of Engineering Physics, École Polytechnique de Montréal, C.P. 6079, Succ. Centre-Ville, Montréal, Québec H3C 3A7, Canada

Note: This paper is part of the APL Photonics Special Topic on Mid-IR Photonics.
[a)]**Author to whom correspondence should be addressed:** oussama.moutanabbir@polymtl.ca

ABSTRACT

There is an increasing need for silicon-compatible high-bandwidth extended-short wave infrared (e-SWIR) photodetectors (PDs) to implement cost-effective and scalable optoelectronic devices. These systems are quintessential to address several technological bottlenecks in detection and ranging, surveillance, ultrafast spectroscopy, and imaging. In fact, current e-SWIR high-bandwidth PDs are predominantly made of III–V compound semiconductors and thus are costly and suffer a limited integration on silicon besides a low responsivity at wavelengths exceeding 2.3 μm. To circumvent these challenges, $Ge_{1-x}Sn_x$ semiconductors have been proposed as building blocks for silicon-integrated high-speed e-SWIR devices. Herein, this study demonstrates vertical all-GeSn PIN PDs consisting of p-$Ge_{0.92}Sn_{0.08}$/i-$Ge_{0.91}Sn_{0.09}$/n-$Ge_{0.89}Sn_{0.11}$ and p-$Ge_{0.91}Sn_{0.09}$/i-$Ge_{0.88}Sn_{0.12}$/n-$Ge_{0.87}Sn_{0.13}$ heterostructures grown on silicon following a step-graded temperature-controlled epitaxy protocol. The performance of these PDs was investigated as a function of the device diameter in the 10–30 μm range. The developed PD devices yield a high bandwidth of 12.4 GHz at a bias of 5 V for a device diameter of 10 μm. Moreover, these devices show a high responsivity of 0.24 A/W, a low noise, and a 2.8 μm cutoff wavelength, thus covering the whole e-SWIR range.

© 2024 Author(s). All article content, except where otherwise noted, is licensed under a Creative Commons Attribution (CC BY) license (https://creativecommons.org/licenses/by/4.0/). https://doi.org/10.1063/5.0197018

26 September 2024 16:56:28

I. INTRODUCTION

Extended-short wave infrared (e-SWIR) photodetectors (PDs) featuring high bandwidth and wide spectrum range are critical to a plethora of applications spanning free-space and fiber-coupled communications, high temporal resolution light detection and ranging (LIDAR), environmental gas sensing, and time-resolved spectroscopy.[1–10] This e-SWIR range (1.5–3 μm) of the electromagnetic spectrum is currently predominately served by compound semiconductors. For instance, the III–V e-SWIR PDs, typically grown on InP or GaSb substrates, can operate at wavelengths exceeding 2.3 μm.[1,11–17] These devices are, however, prone to a limited bandwidth, which remains below 6 GHz. Although the development of GeSn e-SWIR photodetectors is still in its infancy, these semiconductors offer a viable alternative to circumvent the current limitations in both wavelength range and operation speed, in addition to their compatibility with silicon-based complementary metal–oxide–semiconductor (CMOS) technology. Indeed, GeSn is an all-group IV alloy with a demonstrated content-dependent tunable bandgap energy covering the entire e-SWIR and mid-wave infrared (3–8 μm) ranges.[5,18–34]

GeSn PIN PDs can be either free-space or waveguide devices that are directly integrated on Si substrates.[4,5,35–38] Free-space GeSn/Ge PDs with a Sn composition gradient in the active layer have recently shown a bandwidth of 50 GHz and a 2.8 μm cutoff, which highlights the potential of this material system.[39] Notwithstanding this progress, the responsivity of these devices drops significantly at wavelengths above 2.3 μm owing to the remarkable Sn composition gradient and high residual compressive strain that is typical to the GeSn/Ge heterostructures used to implement these PDs. In contrast, the growth of all-GeSn PIN heterostructures can yield thicker yet more relaxed GeSn active layers with uniform Sn composition.[20] These characteristics are needed to achieve a high and uniform responsivity across a larger wavelength range.[40] Up to date, the bandwidth of the demonstrated all-GeSn e-SWIR PDs operating at wavelength exceeding 2.3 μm is limited to 7.5 GHz at

© Author(s) 2024

2.6 μm cutoff wavelength.[41] Herein, this work demonstrates PIN GeSn photodetectors with small active area diameters below 30 μm. These devices are made of vertical all-GeSn PIN PDs consisting of p-$Ge_{0.92}Sn_{0.08}$/i-$Ge_{0.91}Sn_{0.09}$/n-$Ge_{0.89}Sn_{0.11}$ and p-$Ge_{0.91}Sn_{0.09}$/i-$Ge_{0.88}Sn_{0.12}$/n-$Ge_{0.87}Sn_{0.13}$ heterostructures grown on silicon following a step-graded process. It is shown that 12.4 GHz operation at room temperature for a bias of 5 V is achievable by reducing the device diameter down to 10 μm to minimize the total capacitance. The normalized response curves of the PIN devices indicate that the bandwidth is still RC-limited. It is also shown that these devices exhibit a responsivity of 0.24 A/W at 1.55 μm and cutoff wavelength up to 2.8 μm. The responsivity of these devices does not degrade significantly at wavelengths above 2.3 μm, owing to the relaxed all-GeSn heterostructures.

II. RESULTS AND DISCUSSION

A. Growth and characterization of GeSn epilayers

The all-GeSn PIN heterostructures were grown in a low-pressure chemical vapor deposition (CVD) reactor on a 4-inch Si (100) wafer using Ge virtual substrate (Ge-VS). The growth protocol[41] involves the growth of multiple GeSn buffer layers with increasing Sn content to accommodate the lattice mismatch between the device layer and the Ge-VS, followed by PIN growth on top. The two sets of samples were grown at 305 °C with the i-GeSn layer composition of 9 at.% (sample A) and 12 at.% (sample B). The higher Sn content in sample B was obtained by increasing the $SnCl_4$ flow by 40% as compared to sample A. Figure 1 displays a comparison of the structural properties of the as-grown PIN GeSn stacks. The cross-sectional transmission electron micrographs (TEM) in Figs. 1(a) and 1(b) show that dislocations extend to *p*-GeSn layer, while leaving the i-GeSn and n-GeSn regions with higher crystalline quality. Diborane (B_2H_6) and arsine (AsH_3) precursors were used to achieve p- and n-type doping, respectively. The p- and n-layers had carrier concentrations exceeding 1×10^{19} cm^{-3} as determined by capacitance–voltage (C–V) measurements. The composition and strain of the as-grown heterostructures were determined using x-ray diffraction (XRD) Reciprocal Space Mapping (RSM) measurements around the asymmetrical (-2-24) reflection peak. The obtained maps for the 9 and 12 at.% samples are shown in Figs. 1(c) and 1(d), respectively. Both samples exhibit a low residual compressive strain of −0.2% in the buffer layers No. 1–3, while this value slightly increases to −0.3% in the GeSn No. 4 layer. For sample A, the measured residual strain for the PIN layers is −0.11% (p-$Ge_{0.92}Sn_{0.08}$), −0.28% (i-$Ge_{0.91}Sn_{0.09}$), and −0.48% (n-$Ge_{0.89}Sn_{0.11}$), while for sample B, the strain values are −0.19% (p-$Ge_{0.91}Sn_{0.09}$), −0.36% (i-$Ge_{0.88}Sn_{0.12}$), and −0.51% (n-$Ge_{0.87}Sn_{0.13}$).

Furthermore, atom probe tomography (APT) was utilized to map the composition and doping profiles in the as-grown heterostructures down to the atomic level. To facilitate the preparation of the APT tips, chromium (Cr) was deposited on top of the as-grown samples using e-beam evaporation before the focused ion beam processing of the APT specimens. The obtained APT elemental profiles are shown in Figs. 1(e) and 1(f). Starting with the Sn profile, the uniformity of the Sn composition in the GeSn buffer layers and the PIN stack is evident in both samples. The step-wise increase in the Sn content in the four GeSn buffer layers was achieved by reducing the growth temperature in steps of 10 °C during the epitaxial growth. This reduction in temperature

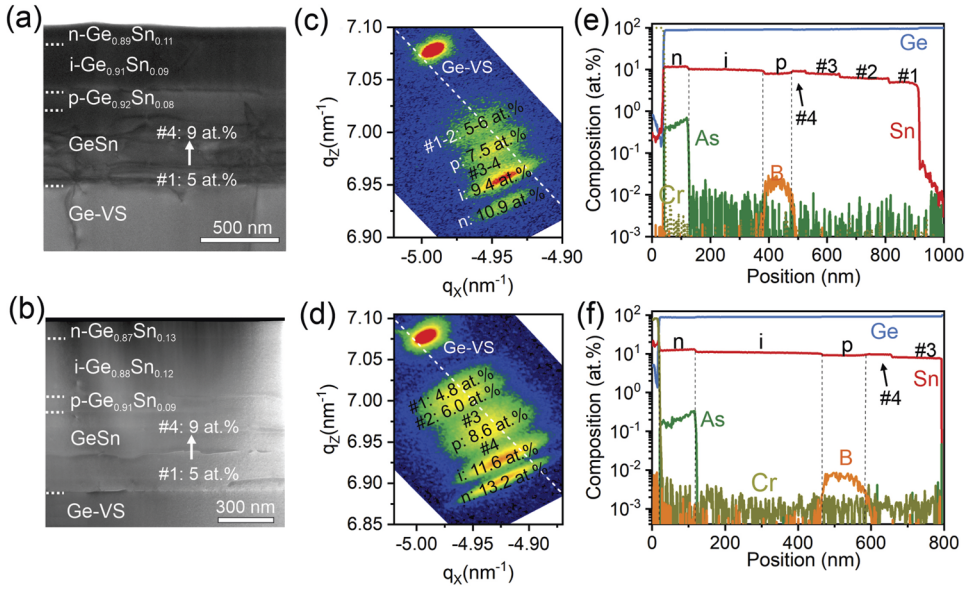

FIG. 1. Structural properties of the as-grown GeSn PIN heterostructures. (a,b) Cross-sectional TEM images of sample A (p-$Ge_{0.92}Sn_{0.08}$/i-$Ge_{0.91}Sn_{0.09}$/n-$Ge_{0.89}Sn_{0.11}$) and sample B (p-$Ge_{0.91}Sn_{0.09}$/i-$Ge_{0.88}Sn_{0.12}$/n-$Ge_{0.87}Sn_{0.13}$), respectively. (c,d) RSM (-2-24) maps for both samples A and B, respectively. (e,f) 3D atom-by-atom reconstructions of the atom probe tips showing the elemental distribution of the As, B, Ge, Sn, and Cr atoms for both samples. Panel (e) was adapted from M. R. Atalla, S. Assali, S. Koelling, A. Attiaoui, and O. Moutanabbir, ACS Photonics **9**, 1425–1433 (2022). Copyright 2022 Author(s), licensed under a Creative Commons Attribution 4.0 License.

26 September 2024 16:56:28

© Author(s) 2024

allows more Sn to be incorporated in the lattice and produces sharp interfaces without any composition gradient. However, the *p*-GeSn layer exhibits a wider interface owing to the slow incorporation of B dopants in the GeSn lattice as evidenced by the gradually increasing B concentration in the *p*-GeSn layer. The n-GeSn is doped by As; however, a careful analysis had to be carried out to decouple the signal of As in the APT mass spectra from that of the Ge due to the small difference between their atomic masses. In addition, it is inferred from Figs. 1(e) and 1(f) that the interface between n-/i-GeSn layers is abrupt and that the Sn content increases as the As dopants are easily incorporated into the lattice of the growing GeSn layer in sharp contrast to the case of B dopants. It is worth mentioning that sample A has higher As and B concentrations as compared to sample B. For instance, the As atomic composition is ~0.6 at.% in the n-layer of sample A compared to just ~0.3 at.% in sample B. In addition, the B atomic composition is ~0.03 at.% in the p-layer of sample A compared to just ~0.01 at.% in sample B. This reduction in the As and B dopant concentrations in sample B is mostly likely related to the increased supply of Sn during the growth of this sample.

B. GeSn PIN photodetectors

Samples A and B were subsequently used to fabricate the PIN PDs following a top–down microfabrication process. The device processing started with an inductively coupled plasma (ICP) Cl_2 etch down to Ge-VS to a depth of ~950 nm followed by a second ICP Cl_2 etch of circular bumps of various diameters down to the p-GeSn layer, which forms a double mesa structure to help isolate every device from its neighboring ones. To passivate the Cl_2-etched sidewall, wet chemical treatment in HCl/HF (1:1) solution for 10 s was used. This is because Ge and tin oxides form at the sidewalls, and it is much better to remove these defective oxides using wet chemistry. Then PECVD deposition of 1.5 μm-thick SiO_2 was performed as an insulation layer. Next, openings in the SiO_2 layer atop the p- and n-GeSn regions were created in a double-step etch consisting of an ICP dry etch of 1100 nm followed by a wet buffered oxide etch (BOE) etch of 400 nm. Finally, a 700-nm-thick Al metal was sputtered, followed by contact patterning and Al wet etch. A scanning electron micrograph (SEM) of a representative 10 μm-diameter device is shown in Fig. 2(a).

The processed PIN devices were then subjected to various sets of electrical and optoelectronic analyses. The recorded I–V curves without illumination are displayed in Fig. 2(b) for both samples A and B for devices with diameters 10, 20, and 30 μm. It is noticeable that sample A has a relatively high rectification ratio around an order of magnitude at 1 V, whereas sample B exhibits a very low rectification ratio approaching unity at the same voltage. This can be attributed to the high defect density in the PIN stack of sample B as compared to sample A, which significantly increases the leak-

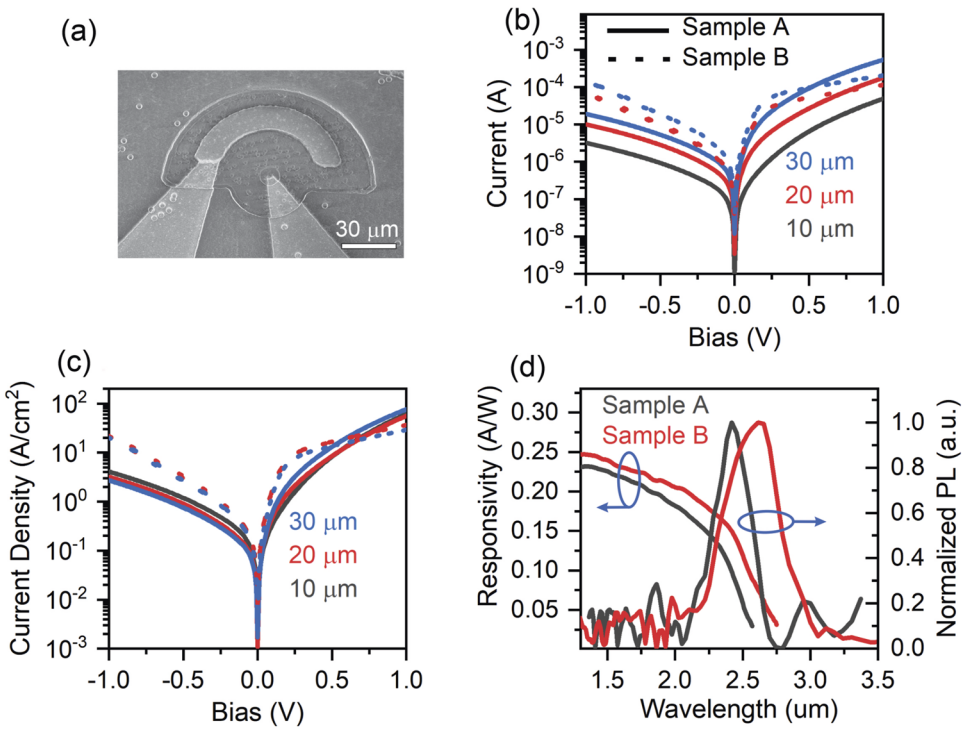

FIG. 2. GeSn PIN photodetectors fabrication and characterization. (a) SEM micrograph of a representative PIN PD with 10 μm in diameter. (b) Room-temperature I–V curves of dark current at various device diameters of sample A compared to sample B. (c) The same as (b) but for the dark current density. (d) Spectral responsivity of sample A compared to that of sample B along with the measured room-temperature PL for both samples.

26 September 2024 16:56:28

© Author(s) 2024

age current as the reverse bias increases. In addition, the relatively lower As composition [Fig. 1(e) and 1(f)] in the n-GeSn of sample B compared to sample A explains the reduced forward bias current of sample B at 1 V. Note that the dark current, which is the PD current under no illumination, increases monotonically as the device diameter increases for both samples in reverse bias. This can be attributed to bulk and/or surface leakage current. In Fig. 2(c), the dark current density is plotted as a function of applied bias, and it shows that it is almost independent of device diameter. This indicates a low surface leakage current and suggests that the bulk leakage in sample B is most likely the reason underlying its high reverse leakage current.

To investigate the device performance under illumination, Fourier transform infrared (FTIR) spectrometer was used to measure the relative spectral responsivity of the PIN GeSn PDs for both samples. The absolute spectral responsivity can be estimated by using a calibrated e-SWIR InGaAs PD. The obtained spectral responsivities of the PIN PDs are plotted in Fig. 2(d) as a function of the incident illumination wavelength. Responsivities of 0.221 and 0.235 A/W were measured at 1.55 μm for both samples A and B, respectively. In both cases, a monotonic decrease in the responsivity is visible until their spectral responsivity reaches cutoff at 2.6 μm (sample A) and 2.8 μm (sample B). It is important to note that the all-GeSn heterostructures are characterized by a uniform high Sn content in the i-layers, thus yielding a high responsivity that reduces only close to the cutoff wavelength. This is a clear advantage of the all-GeSn PIN PDs as compared to GeSn/Ge heterostructures that can suffer from high residual strain and Sn composition gradient, which limit the responsivity as the wavelength increases. The specific detectivity at 2.5 μm wavelength of the 10 μm device (sample B) is calculated[41] to be 2.85×10^8 cm W^{-1} $Hz^{1/2}$ at room temperature, which still has room to improve if the device contact resistance is reduced and the i-layer thickness is increased. The FTIR spectrometer is also used to measure the photoluminescence (PL) spectra of the as-grown samples A and B as displayed in Fig. 2(d). The room temperature PL spectra of samples A and B show peaks at 2.4 and 2.65 μm and their decay extends beyond 2.6 and 2.8 μm, respectively. This strong room-temperature emission rules out any dominating contribution of dislocations to the recorded PL spectra.[42,43] This is consistent with the estimated cutoff wavelength values mentioned previously. It is important to note that the high responsivity and low dark current increase both the PD sensitivity and signal-to-noise ratio, which in turn voids the need for a lock-in technique to extract the photocurrent.[40,41,44]

C. Photoresponse bandwidth of GeSn PDs

There are several factors that affect the photoresponse bandwidth of a PD device. In PIN devices, photocarriers generated outside the depletion region in the n- and p-layers transport to the contacts by diffusion. This diffusion current can slow down the device's photoresponse. Owing to the remarkably short lifetime of photocarriers in GeSn, the diffusion current is most likely too small and shall be neglected in the calculation of the photoresponse bandwidth. In addition, photocarrier trapping and release at the heterojunction interfaces produces a slow photoresponse component; however, this component also reduces as the applied reverse bias increases and shall be neglected as well. Finally, the photocarrier transit lifetime through the depletion region and the resistance–capacitance (RC) delay are considered the main components limiting the photoresponse bandwidth. Consequently, the 3 dB bandwidth, $f_{-3\,\mathrm{dB}}$, can be written as[45,46] $f_{total} = (f_{RC}^{-2} + f_{trans}^{-2})^{-0.5}$, where $f_{RC} = 1/(2\pi \mathrm{RC})$ is the RC-limited bandwidth and R and C are the total resistance and the total capacitance, respectively. The total resistance includes the contact resistance, semiconductor resistance, series resistance, and load resistance, while the total capacitance includes the contacts parasitic capacitance and depletion region junction capacitance. $f_{trans} = 0.45 v_s/d$ is the transit lifetime-limited bandwidth, where v_s is the saturation velocity and d is the i-layer thickness. The transit velocity is estimated using Ge saturation velocity and i-layer thicknesses of 300 and 350 nm for samples A and B, respectively. This limits the photoresponse to 90 GHz (sample A) and 77 GHz (sample B). For the f_{RC}, the series resistance was determined from the forward bias I–V curve to be 120.5 Ω with a load resistance of 50 Ω. The device capacitance was measured for a 10 μm-diameter device to be 0.07 pF at 5 V yielding f_{RC} = 13.34 GHz.

The normalized responses for both samples are measured, and the representative ones are displayed in Fig. 3. The normalized response as a function of frequency for the 20 μm device at various reverse biases is shown in Fig. 3(a). The measurements were

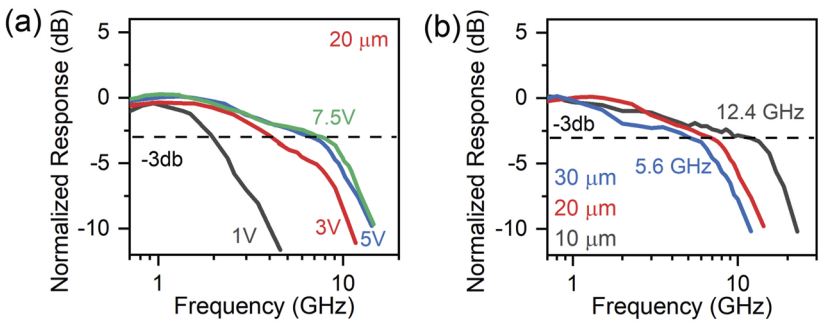

FIG. 3. Photoresponse bandwidth of GeSn PIN PDs. (a) Normalized photoresponse as a function of the incident optical pulse frequency, indicating the photoresponse bandwidth of a 20 μm diameter device at various applied biases. (b) The same as (a) but showing a comparison of the normalized response for the 10, 20, and 30 μm diameter devices at 5 V reverse bias.

26 September 2024 16:56:28

© Author(s) 2024

TABLE I. Comparison of the state-of-the-art high-speed photodetectors operating close to 2.5 μm.

Material	Cutoff wavelength (μm)	Bandwidth (GHz)	Responsivity (A/W)	Current density (A/cm^2) at −1 V	Device
Ge/GeSn	2.5	1.78	0.19 at 1.55 μm	40	Ref. 36
InGaAs/GaAsSb	2.4	3.7	0.35 at 2 μm	0.007	Ref. 14
GaInAsSb	2.4	2–5	1.15 at 2.2 μm	···	Ref. 17
GaInAsSb	2.5	6	0.4 at 1.55 μm	1.63	Ref. 1
All-GeSn	2.6	7.5	0.15 at 2.5 μm	5.4	Ref. 41
Ge/GeSn	2.8	36 (D 10 μm)	0.04 at 2.5 μm	···	[a]Ref. 39
All-GeSn	2.8	12.4 (D 10 μm)	0.18 at 2.5 μm	2.5	This work

[a]Reference 39 reported higher bandwidth devices as well but at much smaller device sizes. In this table, similar size devices are compared.

carried out using a 1.55 μm single-frequency continuous-wave laser that was fiber-coupled to a 40 GHz electro-optical modulator, and the output pulsed light was incident on the PD using a fiber focuser lens. To apply DC bias and an RF signal to the PIN PD and to collect the output current, a bias tee was used along with a parameter analyzer (Keithely 4200A) and a network analyzer (Anritsu 37369D) was used to provide the RF signal. The PIN PD output current is connected to a broadband RF amplifier that amplifies the RF signal before it is fed into the network analyzer input. The −3 dB response values for the 20 μm device at biases of 1, 3, 5, and 7.5 V were 1.95, 3.99, 7.6, and 7.9 GHz, respectively. Below the RC limit, as the reverse bias increases, the capacitance reduces and the device bandwidth increases. The normalized response of PIN devices with different diameters 30, 20, and 10 μm are compared at 5 V, as shown in Fig. 3(b). These devices exhibit a −3 dB response of 5.6, 7.6, and 12.4 GHz, respectively. A comparison of the state-of-the-art high-speed photodetectors operating close to 2.5 μm is provided in Table I. The 10 μm device bandwidth remains below the estimated RC-limited bandwidth value most likely because of the slow diffusion current component contributing to the total device photoresponse.

III. CONCLUSION

This work demonstrates and investigates vertical all-GeSn heterostructures consisting of p-$Ge_{0.92}Sn_{0.08}$/i-$Ge_{0.91}Sn_{0.09}$/n-$Ge_{0.89}Sn_{0.11}$ and p-$Ge_{0.91}Sn_{0.09}$/i-$Ge_{0.88}Sn_{0.12}$/n-$Ge_{0.87}Sn_{0.13}$ heterostructures grown on silicon following a step-graded process. The obtained heterostructures enabled PIN photodetectors to exhibit a high speed reaching 12.4 GHz, low noise, and high responsivity across the whole e-SWIR range. The developed all-GeSn heterostructures offer a viable path to achieve thick, high, and uniform Sn content in the i-layer of the PDs, besides a significant relaxation of the compressive strain that is inherent to these epitaxial materials. Consequently, devices based on these all-GeSn heterostructures exhibit a high and stable responsivity over a broader wavelength range. These characteristics highlight the potential of GeSn PIN PDs as effective building blocks for scalable and silicon-compatible e-SWIR technologies.

ACKNOWLEDGMENTS

The authors acknowledge the support from NSERC Canada (Discovery, SPG, and CRD Grants), Canada Research Chairs, Canada Foundation for Innovation, Mitacs, PRIMA Québec, Defense Canada (Innovation for Defense Excellence and Security, IDEaS), the European Union's Horizon Europe research and innovation program under Grant Agreement No. 101070700 (MIRAQLS), the US Army Research Office Grant No. W911NF-22-1-0277, and the Air Force Office of Scientific and Research Grant No. FA9550-23-1-0763.

AUTHOR DECLARATIONS

Conflict of Interest

The authors have no conflicts to disclose.

Author Contributions

M. R. M. Atalla: Conceptualization (equal); Data curation (equal); Formal analysis (equal); Investigation (equal); Methodology (equal); Writing – original draft (equal); Writing – review & editing (equal). **C. Lemieux-Leduc**: Data curation (equal); Formal analysis (equal); Investigation (equal); Methodology (equal); Writing – review & editing (equal). **S. Assali**: Data curation (equal); Formal analysis (equal); Investigation (equal); Methodology (equal); Writing – review & editing (equal). **S. Koelling**: Data curation (equal); Formal analysis (equal); Investigation (equal); Methodology (equal); Writing – review & editing (equal). **P. Daoust**: Data curation (equal); Formal analysis (equal); Investigation (equal); Methodology (equal); Writing – review & editing (equal). **O. Moutanabbir**: Conceptualization (lead); Funding acquisition (lead); Project administration (lead); Resources (lead); Supervision (lead); Writing – review & editing (lead).

DATA AVAILABILITY

The data that support the findings of this study are available from the corresponding author upon reasonable request.

26 September 2024 16:56:28

© Author(s) 2024

REFERENCES

[1] J.-M. Wun, Y.-W. Wang, Y.-H. Chen, J. E. Bowers, and J.-W. Shi, "GaSb-based pin photodiodes with partially depleted absorbers for high-speed and high-power performance at 2.5 μm wavelength," IEEE Trans. Electron Devices **63**, 2796–2801 (2016).

[2] G. M. Williams, "Optimization of eye safe avalanche photodiode lidar for automobile safety and autonomous navigation systems," Opt. Eng. **56**, 031224 (2017).

[3] I. Kim, R. J. Martins, J. Jang, T. Badloe, S. Khadir, H.-Y. Jung, H. Kim, J. Kim, P. Genevet, and J. Rho, "Nanophotonics for light detection and ranging technology," Nat. Nanotechnol. **16**, 508–524 (2021).

[4] N. Wang, C. Xue, F. Wan, Y. Zhao, G. Xu, Z. Liu, J. Zheng, Y. Zuo, B. Cheng, and Q. Wang, "High-performance GeSn photodetector covering all telecommunication bands," IEEE Photonics J. **13**, 1–9 (2021).

[5] X. Li, L. Peng, Z. Liu, Z. Zhou, J. Zheng, C. Xue, Y. Zuo, B. Chen, and B. Cheng, "30 GHz GeSn photodetector on SOI substrate for 2 μm wavelength application," Photonics Res. **9**, 494–500 (2021).

[6] M. Razeghi and B.-M. Nguyen, "Advances in mid-infrared detection and imaging: A key issues review," Rep. Prog. Phys. **77**, 082401 (2014).

[7] M. Sieger and B. Mizaikoff, "Toward on-chip mid-infrared sensors," Anal. Chem. **88**, 5562–5573 (2016).

[8] H. Lin, Z. Luo, T. Gu, L. C. Kimerling, K. Wada, A. Agarwal, and J. Hu, "Mid-infrared integrated photonics on silicon: A perspective," Nanophotonics **7**, 393–420 (2017).

[9] D. Popa and F. Udrea, "Towards integrated mid-infrared gas sensors," Sensors **19**, 2076 (2019).

[10] B. Chen, Y. Chen, and Z. Deng, "Recent advances in high speed photodetectors for eSWIR/MWIR/LWIR applications," Photonics **8**, 14 (2021).

[11] N. Ye, H. Yang, M. Gleeson, N. Pavarelli, H. Y. Zhang, J. O'Callaghan, W. Han, N. Nudds, S. Collins, A. Gocalinska, E. Pelucchi, P. O'Brien, F. C. Garcia Gunning, F. H. Peters, and B. Corbett, "AlInGaAs surface normal photodiode for 2 μm optical communication systems," in *2015 IEEE Photonics Conf. (IPC)* (IEEE, 2015, pp. 456–459.

[12] A. Joshi and D. Becker, "High-speed low-noise pin InGaAs photoreceiver at 2 μm wavelength," IEEE Photonics Technol. Lett. **20**, 551–553 (2008).

[13] H. Yang, N. Ye, R. Phelan, J. O'Carroll, B. Kelly, W. Han, X. Wang, N. Nudds, N. MacSuibhne, F. Gunning *et al.*, "Butterfly packaged high-speed and low leakage InGaAs quantum well photodiode for 2000 nm wavelength systems," Electron. Lett. **49**, 281–282 (2013).

[14] Y. Chen, X. Zhao, J. Huang, Z. Deng, C. Cao, Q. Gong, and B. Chen, "Dynamic model and bandwidth characterization of InGaAs/GaAsSb type-II quantum wells pin photodiodes," Opt. Express **26**, 35034–35045 (2018).

[15] B. Tossoun, J. Zang, S. J. Addamane, G. Balakrishnan, A. L. Holmes, and A. Beling, "InP-based waveguide-integrated photodiodes with InGaAs/GaAsSb type-II quantum wells and 10-GHz bandwidth at 2 μm wavelength," J. Lightwave Technol. **36**, 4981–4987 (2018).

[16] Y. Chen, Z. Xie, J. Huang, Z. Deng, and B. Chen, "High-speed uni-traveling carrier photodiode for 2 μm wavelength application," Optica **6**, 884–889 (2019).

[17] I. Andreev, O. Y. Serebrennikova, G. Sokolovskii, V. Dudelev, N. Ilynskaya, G. Konovalov, E. Kunitsyna, and Y. P. Yakovlev, "High-speed photodiodes for the mid-infrared spectral region 1.2–2.4 μm based on GaSb/GaInAsSb/GaAlAsSb heterostructures with a transmission band of 2–5 GHz," Semiconductors **47**, 1103–1109 (2013).

[18] O. Moutanabbir, S. Assali, X. Gong, E. O'Reilly, C. Broderick, B. Marzban, J. Witzens, W. Du, S.-Q. Yu, A. Chelnokov *et al.*, "Monolithic infrared silicon photonics: The rise of (Si)GeSn semiconductors," Appl. Phys. Lett. **118**, 110502 (2021).

[19] D. Buca, A. Bjelajac, D. Spirito, O. Concepción, M. Gromovyi, E. Sakat, X. Lafosse, L. Ferlazzo, N. von den Driesch, Z. Ikonic *et al.*, "Room temperature lasing in GeSn microdisks enabled by strain engineering," Adv. Opt. Mater. **10**, 2201024 (2022).

[20] M. R. Atalla, Y. Kim, S. Assali, D. Burt, D. Nam, and O. Moutanabbir, "Extended-SWIR GeSn LEDs with reduced footprint and efficient operation power," ACS Photonics **10**, 1649–1653 (2023).

[21] C.-Y. Chang, P.-L. Yeh, Y.-T. Jheng, L.-Y. Hsu, K.-C. Lee, H. Li, H. Cheng, and G.-E. Chang, "Mid-infrared resonant light emission from GeSn resonant-cavity surface-emitting LEDs with a lateral p-i-n structure," Photonics Res. **10**, 2278–2286 (2022).

[22] J. Chrétien, Q. Thai, M. Frauenrath, L. Casiez, A. Chelnokov, V. Reboud, J. Hartmann, M. El Kurdi, N. Pauc, and V. Calvo, "Room temperature optically pumped GeSn microdisk lasers," Appl. Phys. Lett. **120**, 051107 (2022).

[23] A. Elbaz, D. Buca, N. von den Driesch, K. Pantzas, G. Patriarche, N. Zerounian, E. Herth, X. Checoury, S. Sauvage, I. Sagnes *et al.*, "Ultra-low-threshold continuous-wave and pulsed lasing in tensile-strained GeSn alloys," Nat. Photonics **14**, 375–382 (2020).

[24] Y. Jung, D. Burt, L. Zhang, Y. Kim, H.-J. Joo, M. Chen, S. Assali, O. Moutanabbir, C. Seng Tan, and D. Nam, "Optically pumped low-threshold microdisk lasers on a GeSn-on-insulator substrate with reduced defect density," Photonics Res. **10**, 1332–1337 (2022).

[25] X. Liu, J. Zheng, C. Niu, T. Liu, Q. Huang, M. Li, D. Zhang, Y. Pang, Z. Liu, Y. Zuo, and B. Cheng, "Sn content gradient GeSn with strain controlled for high performance GeSn mid-infrared photodetectors," Photonics Res. **10**, 1567–1574 (2022).

[26] L. Luo, S. Assali, M. R. Atalla, S. Koelling, A. Attiaoui, G. Daligou, S. Martí, J. Arbiol, and O. Moutanabbir, "Extended-SWIR photodetection in all-group IV core/shell nanowires," ACS Photonics **9**, 914–921 (2022).

[27] B. Marzban, L. Seidel, T. Liu, K. Wu, V. Kiyek, M. H. Zoellner, Z. Ikonic, J. Schulze, D. Grützmacher, G. Capellini *et al.*, "Strain engineered electrically pumped SiGeSn microring lasers on Si," ACS Photonics **10**, 217 (2022).

[28] M. R. Atalla, S. Assali, G. Daligou, A. Attiaoui, S. Koelling, P. Daoust, and O. Moutanabbir, "Continuous-wave GeSn light-emitting diodes on silicon with 2.5 μm room-temperature emission," ACS Photonics **11**, 1335 (2024).

[29] G. Daligou, R. Soref, A. Attiaoui, J. Hossain, M. R. Atalla, P. D. Vecchio, and O. Moutanabbir, "Group IV mid-infrared thermophotovoltaic cells on silicon," IEEE J. Photovolt. **13**, 728 (2023).

[30] M. A. Mircovich, C. Xu, D. A. Ringwala, C. D. Poweleit, J. Menéndez, and J. Kouvetakis, "Extended compositional range for the synthesis of SWIR and LWIR $Ge_{1-y}Sn_y$ alloys and device structures via CVD of SnH_4 and Ge_3H_8," ACS Appl. Electron. Mater. **3**, 3451–3460 (2021).

[31] C. Xu, D. Ringwala, D. Wang, L. Liu, C. D. Poweleit, S. L. Chang, H. L. Zhuang, J. Menéndez, and J. Kouvetakis, "Synthesis and fundamental studies of Si-compatible (Si)GeSn and GeSn mid-IR systems with ultrahigh Sn contents," Chem. Mater. **31**, 9831–9842 (2019).

[32] R. Soref, "Enabling 2 μm communications," Nat. Photonics **9**, 358–359 (2015).

[33] Y. Zhou, Y. Miao, S. Ojo, H. Tran, G. Abernathy, J. M. Grant, S. Amoah, G. Salamo, W. Du, J. Liu *et al.*, "Electrically injected GeSn lasers on Si operating up to 100 K," Optica **7**, 924–928 (2020).

[34] J. Chretien, N. Pauc, F. Armand Pilon, M. Bertrand, Q.-M. Thai, L. Casiez, N. Bernier, H. Dansas, P. Gergaud, E. Delamadeleine *et al.*, "GeSn lasers covering a wide wavelength range thanks to uniaxial tensile strain," ACS Photonics **6**, 2462–2469 (2019).

[35] S. Xu, W. Wang, Y.-C. Huang, Y. Dong, S. Masudy-Panah, H. Wang, X. Gong, and Y.-C. Yeo, "High-speed photo detection at two-micron-wavelength: Technology enablement by GeSn/Ge multiple-quantum-well photodiode on 300 mm Si substrate," Opt. Express **27**, 5798–5813 (2019).

[36] H. Tran, C. G. Littlejohns, D. J. Thomson, T. Pham, A. Ghetmiri, A. Mosleh, J. Margetis, J. Tolle, G. Z. Mashanovich, W. Du *et al.*, "Study of GeSn mid-infrared photodetectors for high frequency applications," Front. Mater. **6**, 278 (2019).

[37] E. Talamas Simola, V. Kiyek, A. Ballabio, V. Schlykow, J. Frigerio, C. Zucchetti, A. De Iacovo, L. Colace, Y. Yamamoto, G. Capellini *et al.*, "CMOS-compatible bias-tunable dual-band detector based on GeSn/Ge/Si coupled photodiodes," ACS Photonics **8**, 2166–2173 (2021).

[38] C.-H. Tsai, K.-C. Lin, C.-Y. Cheng, K.-C. Lee, H. Cheng, and G.-E. Chang, "GeSn lateral p-i-n waveguide photodetectors for mid-infrared integrated photonics," Opt. Lett. **46**, 864–867 (2021).

[39] J. Cui, J. Zheng, Y. Zhu, X. Liu, Q. Huang, Z. Liu, Y. Zuo, and B. Cheng, "Sn component gradient GeSn photodetector with 3 dB bandwidth over 50 GHz for extending L band telecommunication," Opt. Lett. **48**, 6148–6151 (2023).

26 September 2024 16:56:28

© Author(s) 2024

[40] H. Tran, T. Pham, J. Margetis, Y. Zhou, W. Dou, P. C. Grant, J. M. Grant, S. Al-Kabi, G. Sun, R. A. Soref *et al.*, "Si-based GeSn photodetectors toward mid-infrared imaging applications," ACS Photonics **6**, 2807–2815 (2019).
[41] M. R. Atalla, S. Assali, S. Koelling, A. Attiaoui, and O. Moutanabbir, "High-bandwidth extended-SWIR GeSn photodetectors on silicon achieving ultrafast broadband spectroscopic response," ACS Photonics **9**, 1425–1433 (2022).
[42] E. Steinmann, "Dislocation luminescence of germanium," Krist. Tech. **16**, 247–250 (1981).
[43] A. Izotov, A. Kolyubakin, S. Shevchenko, and E. Steinman, "Photoluminescence and splitting of dislocations in germanium," Phys. Status Solidi A **130**, 193–198 (1992).
[44] M. R. Atalla, S. Assali, A. Attiaoui, C. Lemieux-Leduc, A. Kumar, S. Abdi, and O. Moutanabbir, "All-group IV transferable membrane mid-infrared photodetectors," Adv. Funct. Mater. **31**, 2006329 (2021).
[45] Y. Dong, W. Wang, S. Xu, D. Lei, X. Gong, X. Guo, H. Wang, S.-Y. Lee, W.-K. Loke, S.-F. Yoon, and Y. C. Yeo, "Two-micron-wavelength germanium-tin photodiodes with low dark current and gigahertz bandwidth," Opt. Express **25**, 15818–15827 (2017).
[46] Y. Lin, K. H. Lee, S. Bao, X. Guo, H. Wang, J. Michel, and C. S. Tan, "High-efficiency normal-incidence vertical p-i-n photodetectors on a germanium-on-insulator platform," Photonics Res. **5**, 702–709 (2017).

26 September 2024 16:56:28

© Author(s) 2024